CellPress

Structure
Resource

Modeling an In-Register, Parallel "Iowa" Aβ Fibril Structure Using Solid-State NMR Data from Labeled Samples with Rosetta

Nikolaos G. Sgourakis,[1] Wai-Ming Yau,[1] and Wei Qiang[1,2,*]
[1]Laboratory of Chemical Physics, National Institute of Diabetes and Digestive and Kidney Diseases, National Institutes of Health, Bethesda, MD 20892, USA
[2]Department of Chemistry, Binghamton University, 4400 Vestal Parkway East, Binghamton, NY 13902, USA
*Correspondence: wqiang@binghamton.edu
http://dx.doi.org/10.1016/j.str.2014.10.022

SUMMARY

Determining the structures of amyloid fibrils is an important first step toward understanding the molecular basis of neurodegenerative diseases. For β-amyloid (Aβ) fibrils, conventional solid-state NMR structure determination using uniform labeling is limited by extensive peak overlap. We describe the characterization of a distinct structural polymorph of Aβ using solid-state NMR, transmission electron microscopy (TEM), and Rosetta model building. First, the overall fibril arrangement is established using mass-per-length measurements from TEM. Then, the fibril backbone arrangement, stacking registry, and "steric zipper" core interactions are determined using a number of solid-state NMR techniques on sparsely ^{13}C-labeled samples. Finally, we perform Rosetta structure calculations with an explicitly symmetric representation of the system. We demonstrate the power of the hybrid Rosetta/NMR approach by modeling the in-register, parallel "Iowa" mutant (D23N) at high resolution (1.2Å backbone rmsd). The final models are validated using an independent set of NMR experiments that confirm key features.

INTRODUCTION

The deposition of amyloid fibrils is a crucial clinical hallmark of a variety of fatal neurodegenerative diseases, including Alzheimer's disease (AD), Huntington's, and Parkinson's disease (Chiti and Dobson, 2006; Selkoe, 1991; Siepe et al., 2012). Specifically for AD, formation of β amyloid (Aβ) fibrils and various oligomers consisting of the 40- or 42-residue Aβ peptides ($A\beta_{1-40}$ or $A\beta_{1-42}$, respectively), correlates with disease progression and has been shown to be toxic to neuron cell cultures (Kayed et al., 2003; Petkova et al., 2005). The $A\beta_{1-40}$ and $A\beta_{1-42}$ segments are derived from the enzymatic cleavage of larger amyloid precursor proteins (APPs) (Barrett et al., 2012; O'Brien and Wong, 2011), and single point mutations of the APP locus are usually associated with familial, early-onset AD (Karran et al., 2011). Characterization of the high-resolution structures of Aβ fibrils has two important impacts to the field of AD. First, it provides crucial information on the molecular mechanism of Aβ amyloid formation process, which is believed to disrupt normal neuronal functions and elicit toxicity (Mason et al., 1996, 1999; Peters et al., 2009; Widenbrant et al., 2006). Second, atomic models could serve as templates for the development of molecules targeting fibril structures, which is one of the clinically tested therapeutic strategies to combat AD (Ladiwala et al., 2012; Petrassi et al., 2000; Sievers et al., 2011).

Biochemical and biophysical characterizations of Aβ fibril structures have been performed extensively during the past two decades (Antzutkin et al., 2000, 2002; Balbach et al., 2000; Benzinger et al., 1998; Bertini et al., 2011; Lansbury et al., 1995; Lu et al., 2013; Paravastu et al., 2008; Petkova et al., 2002, 2006; Qiang et al., 2012; Tycko et al., 2009). These studies typically use aqueous buffers to mimic physiological conditions (*p*H, temperature, and salt concentration) and therefore serve as good in vitro model systems for Aβ fibrils formed around neurons. The sequences of $A\beta_{1-40}$ and $A\beta_{1-42}$ contain two "amyloidogenic" regions at residues 10–22 and 30–40(42) that may form parallel or antiparallel β sheet structures due to their high hydrophobicity (Tycko, 2011). These β sheet structures propagate along the main axis of the fibril, resulting in the characteristic cross-β pattern that is observed in diffraction studies of amyloids (Sunde et al., 1997). An early study by Lansbury et al. (1995) demonstrated that the C-terminal segment of Aβ (named $A\beta_{34-42}$) produces amyloid fibrils with an antiparallel β sheet structure. X-ray crystallography conducted on a number of short Aβ segments (6–8 residues) revealed a polymorphic group of primarily antiparallel β sheet structures, and further highlighted the importance of a "steric zipper" motif, formed by intercalated side chains of hydrophobic residues, in stabilizing the core of the fibril structure (Colletier et al., 2011; Sawaya et al., 2007). However, the longer $A\beta_{10-35}$ segment may also form parallel, in-register β sheet structures (Benzinger et al., 1998). Several studies focusing on $A\beta_{1-40}$ or $A\beta_{1-42}$ have suggested that the parallel in-register structures are the main species of full-length Aβ fibrils (Bertini et al., 2011; Lu et al., 2013; Luhrs et al., 2005; Paravastu et al., 2008; Petkova et al., 2002, 2006). These full-length structures have been proven nonamenable to X-ray diffraction studies, presumably due to the presence of flexible N-terminal and loop segments (residues 1–15 and 23–29) that limit the formation of a well-ordered crystal lattice. Solid-state nuclear

magnetic resonance (NMR) spectroscopy provides a powerful alternative to crystallography for these challenging systems, and several structural models of $A\beta_{1-40}$ fibrils have been determined using a variety of solid-state NMR experiments (Tycko, 2011). These studies revealed a highly diverse range of fibril structures, suggesting that the amyloid state is not uniquely defined by the amyloidogenic sequence, but it is dependent on the precise fibril growth conditions. The types of models that are consistent with the solid-state NMR data include different numbers of cross-β subunits, packing arrangements, and β-stand variations (Lu et al., 2013; Paravastu et al., 2008; Petkova et al., 2006; Qiang et al., 2012). An extreme case of such structural variability is the ''Iowa'' mutant of $A\beta_{1-40}$, consisting of a single amino acid mutation (D23N) that forms mixtures of parallel in-register and antiparallel β sheet fibril structures under physiological buffer conditions, as shown previously by solid-state NMR (Qiang et al., 2012; Tycko et al., 2009). Separation of pure samples of either parallel or antiparallel fibrils was previously achieved using differences in seeding and elongation kinetics between the two species. The antiparallel structure has been shown to be a neurotoxic metastable intermediate (Qiang et al., 2012), suggesting that the interplay between different fibril polymorphs in the brain may have important implications in the progression of familial AD. While a model of the antiparallel structure was previously determined using extensive solid-state NMR restraints from multiple isotopic labeling samples, the parallel structure remains to date.

Given the established polymorphic nature of $A\beta_{1-40}$ fibrils, the availability of detailed structural information would provide the missing link between the observed differences in toxicity and aggregation propensity with atomic features at the molecular level (Petkova et al., 2005). While solid-state NMR has emerged as a powerful technique for providing structural models of amyloid fibrils, high-resolution structure determination typically relies on the collection of a large number of experimental restraints under multiple isotopic labeling schemes that make conventional methods cumbersome. Moreover, due to the presence of alterative fibril symmetries, it is difficult to know a priori what types of experimental restraints are needed to unambiguously determine a structure, or alternatively to assess the range of models consistent with the (sparse) experimental data.

A number of approaches have been applied to model amyloid fibril structures. The first high-resolution structural model for the 40-residue Aβ fibrils (Petkova et al., 2006) was generated using a combination of MOLMOL and TINKER. In that study, complementary experimental constraints were obtained from five scattering uniformly labeled peptides that covered residues 9–40 of the Aβ sequence. Structural modeling was carried out using molecular dynamics (MD) simulations and energy minimization. Other high-resolution Aβ fibril models, such as the three-fold symmetric 40-residue Aβ fibril (Paravastu et al., 2008) and the antiparallel D23N Aβ mutant fibril (Qiang et al., 2012), were generated using similar protocols within the programs AMBER (Cornell et al., 1995) and Xplor-NIH (Schwieters et al., 2003). Structural modeling of Aβ fibrils generated from purified peptides with uniform ^{13}C, ^{15}N isotope labeling has also been performed on both in vitro (Bertini et al., 2011) and brain-seeded fibrils (Lu et al., 2013). More abundant experimental constraints were obtained using the uniformly labeled fibril samples, which facilitated the computational modeling. In addition, a structural model for the 42-residue Aβ fibril was obtained from hydrogen/deuterium exchange data recorded on ^{15}N-uniformly labeled samples (Luhrs et al., 2005) using CYANA (Guntert, 2004).

Here, we describe a modeling approach using the program Rosetta (Leaver-Fay et al., 2011) to model amyloid fibrils from a limited data set of solid-state NMR chemical shifts and distance restraints recorded on sparsely labeled samples. Rosetta modeling has been previously applied to the core HET-s fibrils based on NMR chemical shifts (Skora and Zweckstetter, 2012). Here, alternative fibril arrangements are identified directly on the basis of the experimental data and evaluated explicitly using Rosetta's symmetric modeling framework, allowing for optimal conformational sampling of models under a previously established set of symmetry parameters. The need for extensive restraint data sets is alleviated through the use of a physically realistic energy function. Instead, the sparse NMR data are applied as a means of limiting the global search in areas of conformational space that are close to the correct structure, while the atomic details in the final models are largely defined through a local optimization of the Rosetta energy function. As a result, the final structures display realistic interfaces between monomeric subunits and good structural statistics. We generate a high-resolution fibril model for the parallel, in-register Iowa (D23N) mutant of $A\beta_{1-40}$ using this approach. For this specific familial mutant of Aβ, the only reported fibril structure to date shows an antiparallel arrangement (Qiang et al., 2012). The final models show a reduced steric zipper core and a well-defined loop conformation relative to the mature wild-type fibrils and therefore provide a high-resolution view of an important toxic polymorph to understand the interplay between structure and disease progression for this familial AD.

RESULTS

$A\beta_{1-40}$ D23N Forms a Mixture of Morphologically Distinct Fibrils Grown under the Same Experimental Conditions

The experimental procedure used to obtain homogeneous parallel D23N $A\beta_{1-40}$ fibrils is outlined in Figure 1A. Starting from an initial mixture containing both parallel and antiparallel fibrils, we took advantage of previously observed differences in nucleation and elongation kinetics between the two species (Qiang et al., 2012). In particular, the antiparallel fibrils show faster nucleation/slower elongation phases relative to the parallel fibril species. First, we generated a mixture of short fibril fragments, of approximately 50–100 nanometers (nm) in length by sonication. We then added an excess of monomeric D23N $A\beta_{1-40}$ peptides, leading to seeded fibril growth using the initial short fragments as templates. We have previously shown that the antiparallel fibril structure can be isolated using a similar iterative filtration/generation seeding protocol (Qiang et al., 2012). The key step in that study was to separate the antiparallel fibril from other components in the mixture based on its distinct size. Here, we used fast generation seeding protocols involving repeated sonication and incubation cycles in a relatively short time course to selectively amplify the kinetically favored parallel structure. Figure 1B shows a representative transmission electron microscopy (TEM) image obtained for the parallel fibrils after 8-cycles of fast generation seeding. The filaments display a uniform long

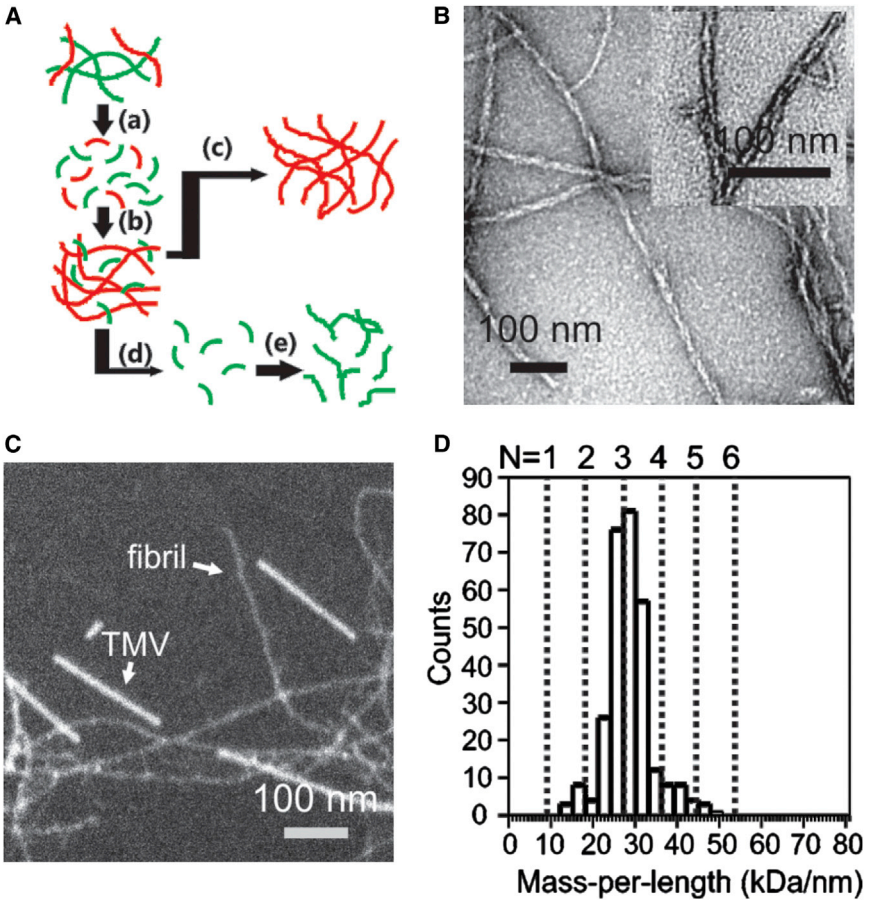

Figure 1. Preparation and TEM Characterizations of the Parallel Iowa Mutant Fibrils

(A) Scheme for purifying the mixture of D23N $A\beta_{1-40}$ fibrils that contain both parallel (red) and antiparallel (green) structures. The detailed protocols are (a) sonication for 2 min in ice bath, (b) quiescent incubation at 4°C for 4 hr, (c) repetition of the steps (a) and (b), (d) filtration with 0.22 μm filter, and (e) quiescent incubation 4°C for 24 hr.

(B) Negatively-stained TEM image of the parallel D23N $A\beta_{1-40}$ fibril.

(C) Tilted-beam TEM image of D23N $A\beta_{1-40}$ fibril for MPL measurement. Arrows indicate images of fibrils.

(D) Histogram of the mass-per-length (MPL) distribution of parallel D23N $A\beta_{1-40}$ fibril. The plot was generated based on 300 individual MPL measurements. The distribution fit to a single Gaussian function with the peak value n = 3, indicating a bundle of three cross-β subunits per layer.

and straight morphology that is clearly distinct from the short and curvy morphology of previously identified antiparallel D23N $A\beta_{1-40}$ fibrils (Qiang et al., 2012). In addition, this morphology is clearly distinct from the two most commonly observed morphologies of wild-type $A\beta_{1-40}$ fibrils, named twisted sheet and striated ribbon (Paravastu et al., 2008; Petkova et al., 2006). The majority of filaments were single and unbundled, with rough surfaces and irregular twisting. These novel features suggest that the underlying atomic structure of D23N fibrils is also distinct from wild-type $A\beta_{1-40}$, consistent with our previous observation that there was no cross seeding effect between D23N mutant and wild-type fibrils (Qiang et al., 2012).

A representative tilted-beam TEM image and derived mass-per-length histogram are shown in Figures 1C and 1D, respectively. Together with the established regular symmetry by NMR (as outlined in the following section), these results suggest a three-fold symmetry axis (N = 3 subunits/layer) for the parallel D23N $A\beta_{1-40}$ fibrils, where each filament is a bundle of three cross-β subunits. The apparent distribution range from 2–4 subunits per layer in Figure 1D is likely due to background scattering in the dark field images (Lu et al., 2013). We have previously shown that antiparallel D23N fibrils formed under the same experimental conditions display a primarily single-layer structure, suggesting that the antiparallel fibril is a metastable intermediate rather than a mature fibril (Qiang et al., 2012). On the other hand, the parallel fibrils studied here contain multiple subunits, which is a common feature of mature Aβ fibrils formed by the wild-type peptides (Lu et al., 2013; Paravastu et al., 2008; Petkova et al., 2006).

The Backbone Conformations of D23N $A\beta_{1-40}$ in Parallel and Antiparallel Fibrils Are Highly Similar

As a probe of the local secondary structure of parallel D23N $A\beta_{1-40}$ fibrils, we measured backbone ^{13}C chemical shifts. We used the finite-pulse radio frequency-driven recoupling (fpRFDR) experiment to record 2D spectra for a series of Aβ fibril samples prepared with the scattering uniformly labeling approach that involves isotopic labeling for at most one residue in the polypeptide sequence per amino acid type. This labeling scheme (Figure 2A) was necessary to reduce spectral overlap, while still providing a sufficient number of labeled sites in the two commonly observed hydrophobic core regions of Aβ. A representative 2D ^{13}C-^{13}C correlation spectrum is shown in Figure 2B. Most of the labeled residues show only one set of crosspeaks, with the exception of G29 and A30, which have one major and one minor component. This observation suggests that, after eight cycles of generation seeding, the sample becomes highly homogeneous and further highlights the presence of regular symmetry in the fibril structure (i.e., an identical chemical environment for all equivalent Aβ subunits). Inspection of the secondary chemical shift values (Wishart et al., 1995) suggests that there are two well-defined β strands, spanning residues K16–A21 and A30–V36 (Figure 2C). The chemical shifts of V39 are also consistent with a β strand conformation. However, the Cα/Cβ crosspeak intensity is clearly weaker relative to other residues, suggesting that there may be more motion within the C-terminal region (Figure 2B). Similar to the previously determined antiparallel D23N $A\beta_{1-40}$ fibril (Qiang et al., 2012), the parallel fibril shows a relatively shorter C-terminal hydrophobic core region relative to the wild-type Aβ fibrils,

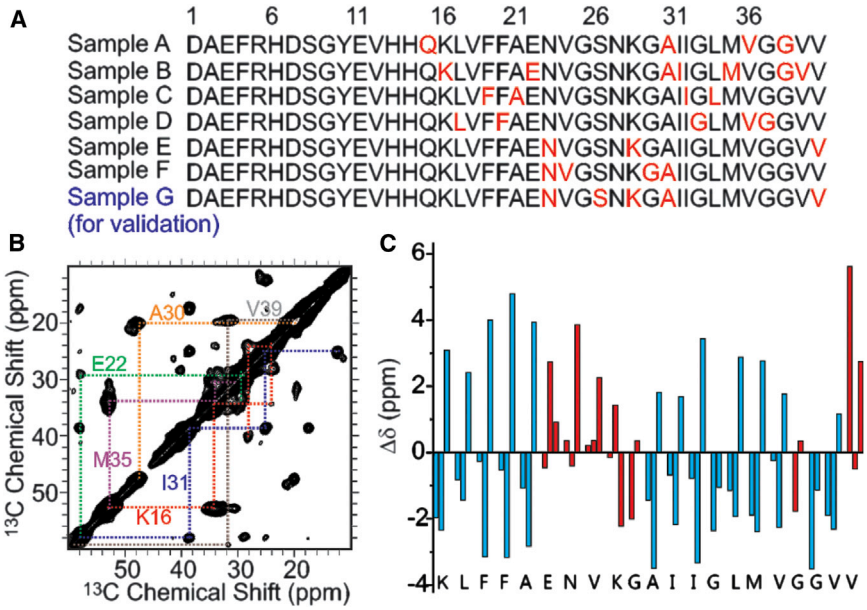

Figure 2. Secondary Chemical Shifts for the Parallel Iowa Mutant Fibrils

(A) Isotopic labeling schemes for the scattering uniform labeled samples. The ^{13}C, ^{15}N-labeled amino acids are shown in red. Fibril structures were determined from NMR experiments on samples (A–F). The labeling pattern shown in (G) was synthesized to validate the structural model.

(B) The aliphatic region of a representative 2D ^{13}C-^{13}C fpRFDR spectrum (sample B) of the parallel D23N $A\beta_{1-40}$ fibril. The assignments of different residues are shown with connections between the corresponding crosspeaks.

(C) Plot of the secondary chemical shifts of the isotopically labeled residues. For each residue, the bars indicate $\Delta\delta$ of C', Cα, and Cβ from left to right, respectively. Based on the secondary chemical shifts, the residues with typical β strand secondary structure (negative C', Cα, and positive Cβ) are shown in blue, while other residues are shown in red.

according to analysis of backbone chemical shifts (cf. Table S2 available online). This trend is also evident in the predicted backbone torsion angles using TALOS+ (Table 1) (Shen et al., 2009). The comparison between the backbone Cα and Cβ chemical shifts for parallel versus antiparallel D23N fibrils suggested that the two species share a similar backbone conformation, probably with the exception of E22, where the parallel fibrils seem to adopt a more α-helical-like conformation (Table S2).

The Parallel D23N $A\beta_{1-40}$ Fibrils Demonstrate an Extended Hydrophobic Core Relative to the Antiparallel Structure

We used a variety of solid-state NMR methods to measure long-range interactions, arising from contacts both within a single Aβ subunit and across different trimeric layers. Figures 3A and 3B show the ^{13}C-PITHIRDs-CT decay curves, which report on distances between specific labeled sites on adjacent monomers along the fibril axis. The ^{13}C isotopic label was placed on the carbonyl carbons of V18 or M35, or the methyl carbons of A21 or A30. These residues are located within the β strand regions according to the chemical shift analysis (Figure 2C). The decay curves fit approximately to a 5.0 ± 0.3Å distance, which corresponds to the expected distance between these atoms in an ideal parallel, in-register β sheet structure (Figure 3C). The fact that the experimental decay curves for all four sites are indistinguishable within the experimental uncertainty suggests that the intersubunit β sheet pairing extends over the entire length of the N- and C-terminal strands. This trend is clearly different from the similar experiments performed previously using antiparallel D23N $A\beta_{1-40}$ fibrils, where similar labeling sites showed much slower 13C-PITHIRDs-CT decay curves (Qiang et al., 2012). Electron diffraction measurements on the parallel fibril sample show a clear diffraction ring at 4.8 Å, further indicating a strong cross-β fibril structure in agreement with the NMR results (Figure S2).

We then recorded radio frequency assisted diffusion (RAD) spectra reporting on long-range ^{13}C-^{13}C internuclear distances between 3–7 Å (Figure 4). A commonly observed structural motif in amyloid fibrils is the "U-like" conformation, where the two sequential β strands are packed against each other forming a steric-zipper core of hydrophobic side-chain contacts (Sawaya et al., 2007). Comparison between fully labeled and diluted samples (shown in Figures 4A and 4B, respectively) suggests that, in the D23N $A\beta_{1-40}$ fibrils used here, such interactions are not intramolecular, but intermolecular (Petkova et al., 2006). For the diluted samples, the fibrils were prepared using the same procedure, but with a 5:1 molar ratio of supplied unlabeled and labeled Aβ peptides in order to suppress intermolecular contacts between the labeled sites. Representative slices in Figure 4E show that the interactions between the aromatic carbons of F19 to L34 Cγ and A21 Cα to I32 Cγ1 were significantly attenuated in the diluted sample, suggesting the presence of an intermolecular polarization transfer pathway. In particular, these interactions are likely formed between the N-terminal β strand (K16–A21) of one monomer and the C-terminal strand (A30–V36) of the adjacent monomer along the fibril axis. Furthermore, we observed that most of the intraresidue crosspeaks for I32 were eliminated in the diluted samples. However, similar effects were not detected for residues F19, A21, and L34, suggesting that the I32 methyl carbons may have shorter spin-lattice relaxation time values such that the signal is attenuated during the long RAD mixing period. The same effect was not observed in experiments recorded for the undiluted sample, likely due to the presence of additional labeling sites near I32 that may restore the signal through polarization transfer. Additional RAD spectra allowed the identification of an unusual long-range contact between L17 and V36 (Figure S3), suggesting that the hydrophobic core of the parallel fibril structure is more extended relative to the antiparallel fibril (Qiang et al., 2012), but less extended than in wild-type fibrils, where the C-terminal β sheet reaches the end of the polypeptide chain (Petkova et al., 2006).

Table 1. Chemical Shifts of the Parallel D23N $A\beta_{1-40}$ Fibril and the Predicted Backbone Torsion Angles Using TALOS+

Residues	C (ppm)	Cα (ppm)	Cβ (ppm)	Cγ (ppm)	Cδ (ppm)	Cε/Cζ (ppm)	Torsion Angles (Φ,φ)
K16	172.9 (174.9)[a]	52.2 (54.5)	34.5 (31.4)	23.8	27.8	39.9 (Cε)	
L17	175.1 (175.9)	52.0 (53.4)	43.1 (40.7)	26.3	23.1 (δ1, δ2)[b]		−110.8 (14.3), 124.5 (7.6)[c]
F19	173.8 (174.1)	52.9 (56.0)	41.9 (37.9)			128.5 (Cζ)	−119.0 (13.6), 146.6 (12.6)
F20	173.6 (174.1)	52.8 (56.0)	42.7 (37.9)			128.9 (Cζ)	−130.0 (11.4), 147.8 (12.9)
A21	175.0 (176.1)	48.0 (50.8)	21.3 (17.4)				−131.1 (16.2), 141.1 (14.1)
E22	174.5 (174.9)	57.6 (54.9)	29.1 (28.2)	33.0	180.3		−81.8 (15.9), −28.0 (8.4)
N23	173.8 (173.5)	51.0 (51.4)	41.0 (37.2)	177.2			−111.4 (36.6), 149.3 (12.4)
V24	174.8 (174.6)	60.8 (60.5)	33.4 (31.2)	18.0 (γ1) 16.5 (γ2)			
K28	174.8 (174.9)	55.9 (54.5)	33.4 (31.4)	25.3	29.4	40.2	
G29	171.2 (173.2)	43.8 (43.4)					−112.1 (67.4), 129.7 (32.9)
A30	174.7 (176.1)	47.3 (50.8)	19.2 (17.4)				−127.4 (17.3), 146.6 (15.3)
I31	174.0 (174.7)	57.2 (59.4)	38.8 (37.1)	24.7 (γ1), 17.1 (γ2)	12.2		−120.1 (11.4), 127.9 (6.0)
I32	173.9 (174.7)	56.1 (59.4)	40.5 (37.1)	24.8 (γ1), 15.7 (γ2)	11.4		−122.0 (12.5), 148.9 (15.7)
G33	170.9 (173.2)	42.4 (43.4)					−125.5 (16.5), 147.2 (13.6)
L34	174.8 (175.9)	51.5 (53.4)	43.6 (40.7)	24.3	21.0 (δ1, δ2)		−118.0 (12.5), 129.4 (12.2)
M35	172.7 (174.6)	51.3 (53.7)	34.0 (31.2)	30.5			−127.6 (17.2), 132.8 (10.8)
V36	174.4 (174.6)	58.3 (60.5)	33.0 (31.2)	19.6 (γ1) 17.8 (γ2)			−120.2 (16.4), 137.8 (20.3)
G37	171.4 (173.2)	43.7 (43.4)					171.9 (65.6), 172.2 (24.8)
G38	169.7 (173.2)	42.3 (43.4)					−126.1 (21.5), 144.0 (12.5)
V39	172.9 (174.6)	58.2 (60.5)	32.4 (31.2)	19.3 (γ1 and γ2)			−124.5 (25.7), 134.5 (21.1)
V40	169.0 (174.6)	60.0 (60.5)	33.9 (31.2)	20.4 (γ1 and γ2)			

[a]Chemical shift values for the random coil conformation.
[b]The peaks for Cγ1 and Cγ2 were not resolved in NMR spectrum. Similar signal overlapping was observed for the side chains of L34, V39, and V40.
[c]Uncertainty given by the TALOS+ program.

Specific interactions involving residues in non-β strand regions provide additional information toward deriving atomic models of fibril structures. The loop region (E22–G29) is highly ordered according to the observed NMR line widths (i.e., ~200 Hz) that are similar as for residues in the β strand regions. Figures 4C and 4D show an important interaction in this region, as revealed by multiple crosspeaks. Several ^{13}C nuclei along the K28 side chain are in close proximity with the CO and Cβ of the C-terminal V40. However, a possible salt bridge interaction between the Nε of K28 and CO of V40 was not observed in additional NMR experiments (Figure S4A), suggesting that the side chain of K28 is likely to be solvent-exposed. Similar interactions between K28 and V40 were observed for the antiparallel D23N $A\beta_{1-40}$ fibril, but not for fibrils formed by wild-type Aβ (Paravastu et al., 2008; Qiang et al., 2012). Notably, several wild-type Aβ fibrils show a salt bridge contact between D23 and K28, suggesting that the side chain of K28 is oriented toward the hydrophobic core of the fibril (Ahmed et al., 2010; Lu et al., 2013; Petkova et al., 2006). Therefore, the single D23N mutation likely affects the local backbone torsion angles in the loop region causing a side-chain flip for K28, a residue that has been proposed to play an important role during the initial steps of the fibril formation process (Reddy et al., 2009; Tarus et al., 2006). To further verify the absence of N23/K28 interaction in the mutant fibril, we performed additional ^{15}N-^{13}C rotational-echo double resonance experiments on the residue pairs N23 C'/K28 Cε and N23 Cγ/K28 Cε. The negative results shown in Figure S4B indicated that these sites are in the fibril structure.

Structure Modeling Using Rosetta Reveals a Staggered β Sheet Arrangement and Extended Hydrogen Bond Network Involving Asn23

To generate atomic models of the filament core structure, we used an explicit Rosetta symmetric modeling framework (DiMaio et al., 2011), further extended to fibril systems with additional point symmetries. Starting from a fibril arrangement consisting of nine trimers of $A\beta_{15-40}$ polypeptide chains in a fully extended conformation, we optimized the total energy of the system, including the solid-state NMR restraints, by simultaneously sampling both the internal backbone degrees of freedom and the six rigid body degrees of freedom defining the overall fibril topology (Das et al., 2009). We used the conformation-dependent chemical shifts to select 3- and 9-residue backbone fragments from high-resolution structures in the Protein Data Bank (PDB) that were then assembled into full $A\beta_{15-40}$ polypeptide chains (Vernon et al., 2013). Backbone and rigid-body changes were propagated among symmetry-related subunits, thus limiting conformational search and energy evaluations to models that are consistent with the overall symmetry of the system. Finally, we used symmetric full-atom refinement to optimize the placement of side-chain rotamers through Monte-Carlo trials and gradient-based minimization of all backbone, side-chain, and rigid-body degrees of freedom. The weight of the solid-state NMR restraints at this final refinement stage was reduced to 1/10 of the original value, such that the final atomic features of the models are defined according to a physically realistic all-atom energy function (Leaver-Fay et al., 2011). The explicitly

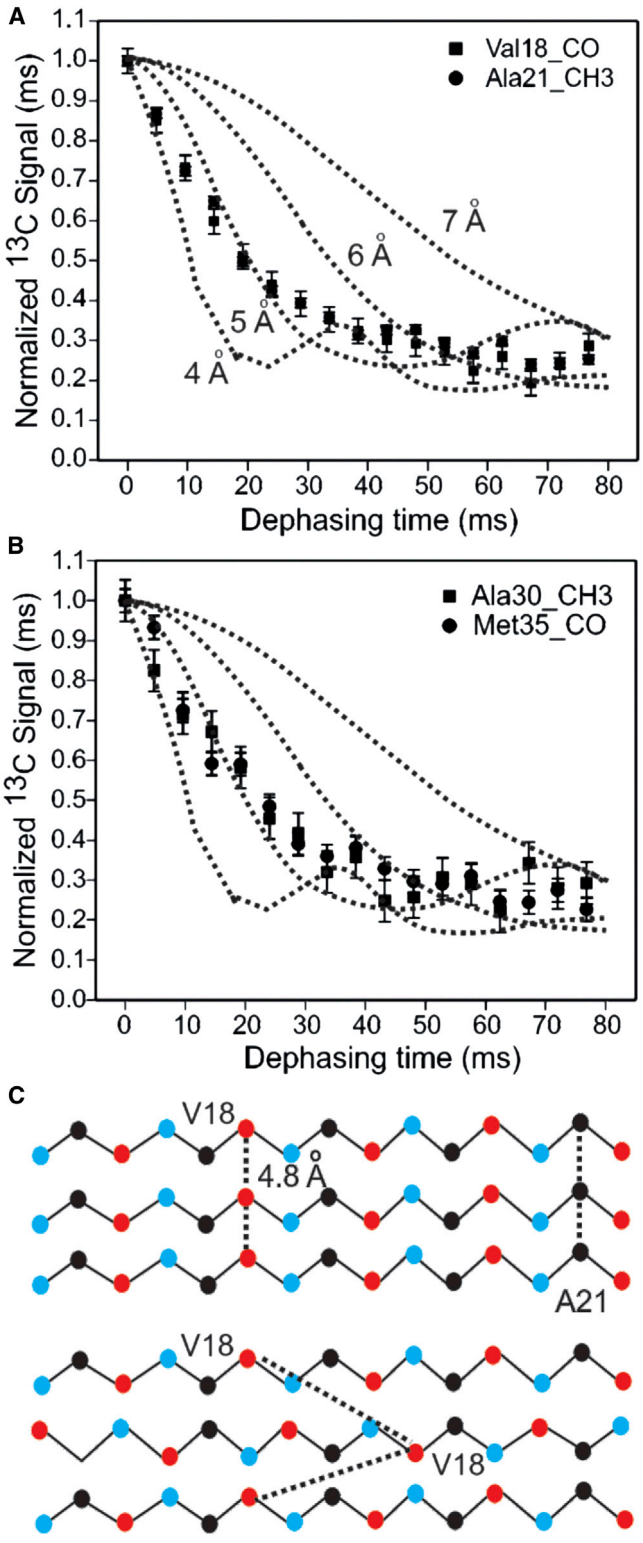

Figure 3. PITHIRDs Measurements on Backbone Registry

(A and B) ^{13}C PITHIRDS dephasing curves for selectively labeled sites in parallel D23N Aβ_{1-40} fibril. In (A) and (B), the error bars were estimated from the spectral noises in the corresponding PITHIRDs spectra.

(A) Val18 CO and Ala21 CH_3.

(B) Ala30 CH_3 and Met35 CO. The theoretical dephasing curves calculated for different internuclear distances are shown as dotted lines. All labeled residues have dephasing curves that fit to ~5 Å simulated distance.

(C) Schematic presentation of the parallel and antiparallel β sheet backbone composed of residues 17–21. The amide N, Cα, and C' were shown in blue, black, and red, respectively. The dotted lines in the parallel scheme indicated the interstrand distance of ~4.8 Å that can be detected using PITHIRDs (cf. A), while the same antiparallel scheme was too long to be measured.

symmetric representation of the system used here allows for a tractable search of the six rigid-body degrees of freedom that uniquely define a fibril arrangement in a systematic manner (Figure S5).

The ten lowest-energy models that show no major violations of the solid-state NMR restraints were selected for deposition in the PDB (PDB ID 2MPZ; Table 2). This final ensemble of models is highly converged at the protofilament level (within 1.15/1.45 Å backbone heavy atom rmsd). The fold of individual subunits consists of a typical β-loop-β structure, with the two β strands spanning residues K16–N23 and A30–V36 (Figure 5A), consistent with the Cα secondary chemical shift pattern (Figure 3C). Notably, the core of the structure is stabilized by a steric zipper motif formed between the side chains L17, F19, and A21 from monomer i that interdigitate between the side chains of I32, L34, and V36 from monomers i and i+3, thus explaining the weakening of crosspeaks between these residues in the NMR dilution experiments. When viewed alongside the fibril axis, adjacent Aβ monomers display a staggered β pattern, allowing the formation of the intra and intermolecular steric zipper (Figure 5B). The staggered arrangement results from an axial displacement of the outer β strand by 0.5 layers (+0.5) per subunit, which gives rise to an intermolecular pattern of side-chain packing interactions. The structure of the loop region at residues ^{24}VGSNK^{29}G shows key side chain and hydrogen bonding features. In particular, while the side chains of N27 and K28 are oriented toward the exterior of the structure, N23 and S26 are facing toward the core of the fibril. In particular, N23 is forming a string of intermolecular hydrogen bonds parallel to the main axis of the fibril, and S26 helps stabilize the loop conformation through a side-chain-to-backbone hydrogen bond to the amide group of N27 (Figure 5C). The side-chain placement of the loop residues were validated using additional solid-state NMR 2D ^{13}C-^{13}C spin diffusion experiments with uniform labeling at residues N23, S26, K28, A30, and V40, where strong crosspeaks were observed between N23 and S26 as predicted by the Rosetta models (Figure S6A). The new, high-resolution spectra further confirmed the presence of multiple close contacts between residues K28 and V40. For instance, the crosspeaks for the pairs K28 Cε/V40 Cγ, K28 Cδ/V40 Cγ, and K28 C'/V40 Cγ can be assigned unambiguously (Figure S6B). Notably, the final structure showed closer contacts between these additional nuclei pairs than the contacts that were utilized as structural restraints (Table S1). Contacts used in the Rosetta modeling typically had unambiguous assignments with high signal-to-noise ratio in the NMR spectra. A few close contacts suggested by the structural model, such as E22 Cα/A30 Cβ, cannot be assigned due to signal overlap in the spectra nuclei pairs, including G29 Cα/N23 Cβ and G38 Cα/I31 Cγ2, showed relatively weak crosspeaks and were therefore not used as structural restraints.

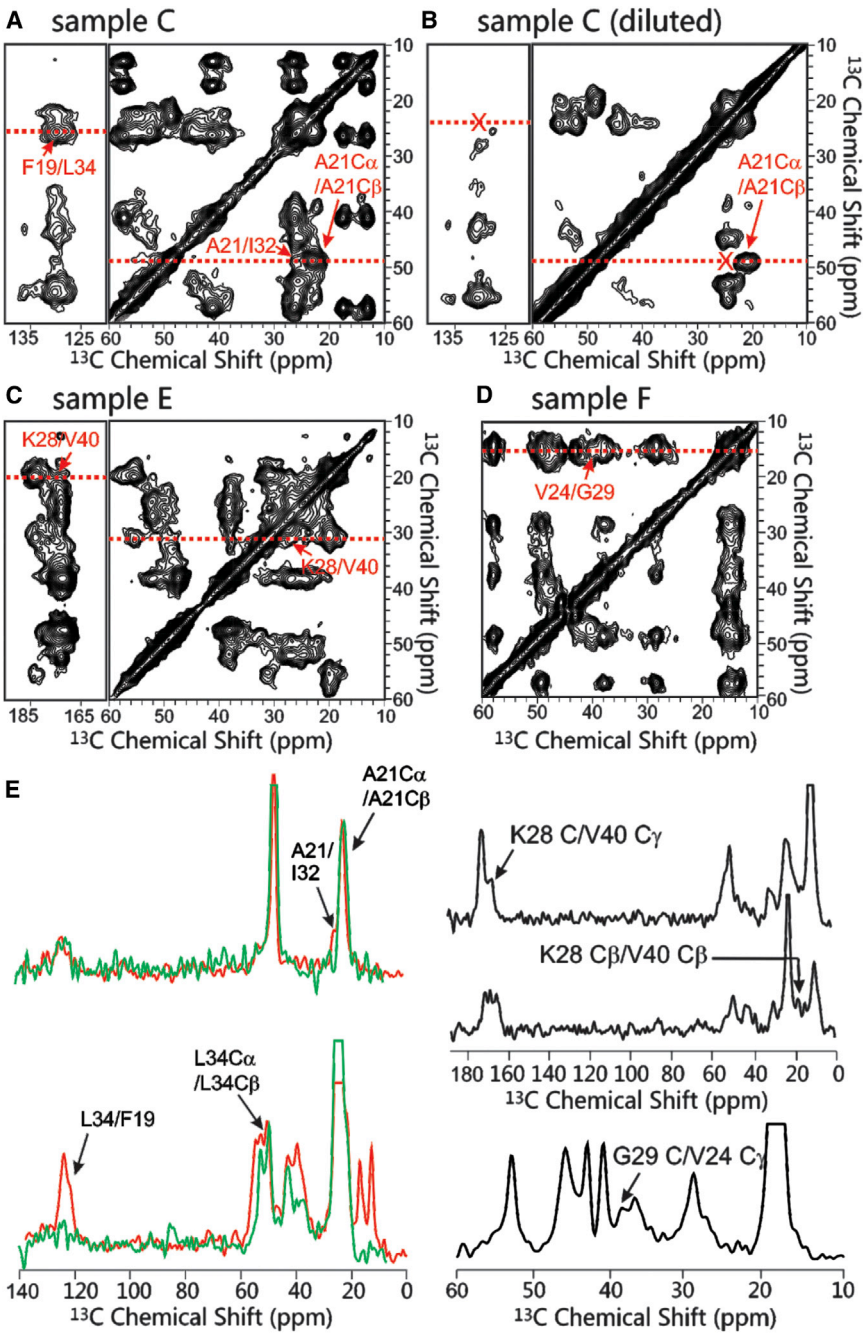

Figure 4. Representative 2D ^{13}C-^{13}C RAD Spectra

(A–D) The sample was prepared by diluting the labeled $A\beta_{1-40}$ peptide with unlabeled peptide in 1:5 molar ratio. The crosses in (B) indicate that the F19/L34 and A21/I32 interactions missing (A), suggesting that these crosspeaks result from interstrand contacts.

(E) The intraresidue crosspeaks in the diluted (green) and undiluted (red) specra were the same intensity to facilitate the direct comparison for the interresidue crosspeaks.

(F) Red arrows indicate important crosspeaks that long-range restraints.

DISCUSSION

Several studies focusing on structural characterization of Aβ fibrils have been carried out over the past two decades, with a number of models proposed for fibrils of different lengths and sequence mutations, under a range of experimental and sample preparation conditions (Bertini et al., 2011; Lu et al., 2013; Luhrs et al., 2005; Paravastu et al., 2008; Petkova et al., 2006; Qiang et al., 2012). This body of work strongly suggests that different Aβ fibrils vary significantly in terms of their overall symmetry parameters, the extent of the β sheet hydrophobic core, the main chain hydrogen bonding patterns, and the detailed side-chain packing interactions within the core steric zipper. An important question is whether the observed differences at the structure level may lead to different toxicities, tissue localization, or other functional properties, as suggested by recent studies using rat embryonic neurons (Petkova et al., 2005). To address this fundamental problem, further development of high-resolution structure determination methods is required. Solid-state NMR is a powerful technique to gain atomic-level information on these insoluble, noncrystalline systems, however, the collection of complete restraint data sets required for conventional structure determination protocols is often limited by spectral overlap that reduces the number of well-resolved resonances in the spectra of fully labeled fibril samples.

Our modeling of the Iowa mutant Aβ fibril makes use of a combination of solid-state NMR data recorded on sparsely labeled samples with Rosetta symmetric modeling, providing a good example of obtaining high-resolution structural models from limited experimental restraints. Spectral overlap is reduced using a sparse labeling approach, with the introduction of ^{13}C and ^{15}N labels at selected sites of the amino acid sequence. The method overcomes low restraint count (cf. Figure S7, ~1–2 experimental long-range restraints per residue used in this study) by exploiting a physically realistic, all-atom energy function that is sensitive to hydrogen bonding and side-chain packing interactions. As a result, the final models show realistic structural features at a resolution that is significantly higher than can be afforded by the available experimental data.

While the solid-state NMR backbone chemical shifts help define the local backbone conformation and long-range packing interactions, an additional source of valuable structural

Table 2. Solid-State NMR Restraints and Structural Statistics

NMR Distance and Dihedral Angle Restraints	
Total distance restraints	43
Intramonomer (long-range)	15/6[a]
Intermonomer	9/1
Hydrogen bonds[b]	12
Total dihedral angle restraints[c]	44
Φ	22
Ψ	22
Structural statistics (residues 15–40)[d]	
Ramachadran outliers	0%
Ramachadran favored	96%
Generously allowed	4%
Restraint violations (used/validation)	1/0
MOLPROBITY clashscore, all atoms[e]	10.65
Average rmsd (Å)[c]	
Backbone[f]	1.2/1.5
All heavy atom[f]	1.9/2.2

[a]Numbers indicate the restraints used for structure calculation/validation.
[b]Inferred from the combination of the cross-β diffraction patterns, the backbone chemical shifts, and ^{13}C-PITHIRDs-CT experiments.
[c]Used to bias the selection of 3-mer and 9-mer backbone fragments, as outlined in Experimental Procedures.
[d]Computed over the five lowest-energy structures.
[e]Clashscore is the number of serious steric overlaps (>0.4 Å) per 1,000 atoms.
[f]Reported for a monomer/lateral dimer respectively, as outlined in Figure 5.

information comes from the observation of a single NMR resonance for every labeled atom. Given the high degree of sensitivity of the chemical shifts to the local conformation of the polypeptide chain (Shen et al., 2009), this suggests that the NMR sample consists of homogeneous fibrils at the atomic level (consistent with the uniform appearance of fibril morphologies under the electron microscopy [EM]), and strongly supports the presence of regular symmetry in the fibril structures, where adjacent Aβ subunits have identical backbone dihedrals and side-chain rotamers. These symmetry considerations provide an additional structural constraint that reduces significantly the extent of conformational space to be searched. Here, we exploit this information by using an explicitly symmetric representation of the system that further limits sampling to conformations that satisfy the fibril and point symmetries of the system, as determined experimentally from TEM mass-per-length measurements. In summary, the use of an explicit representation of symmetry significantly reduces the number of structural constraints needed.

The overall organization of subunits around the 3-fold axis of symmetry reveals a luminal orientation of the C-terminal β strand at an intermediate resolution (backbone rmsd of 4.8 Å, computed along the 3-fold symmetry axis). While the sharp resonances of residues involved in intermolecular contacts along the 3-fold axis suggest the lack of conformational variability, a number of possible rigid-body orientations are consistent with the sparse solid-state NMR restraints. However, the spectra clearly indicate multiple interactions between V40 and K28 that can only be satisfied by an intermolecular contact between these residues. These restraints are sufficient to obtain convergence on a bundle of subunits that interact laterally through the loop and C-terminal regions facing the center of the fibril, while the N-terminal β strand forms the exterior of the fibril structure. Using the new Rosetta modeling framework with additional structural restraints from solid-state NMR and high-resolution cryo-EM density data will enable a more rigid-body placement of the individual subunits toward a complete atomic model of the higher-order fibril structure.

Despite their common parallel β sheet arrangement and 3-fold symmetry axis, our results show notable differences between the D23N and wild-type $A\beta_{1-40}$ fibrils. A clear difference between the two structures involves the size of hydrophobic core, i.e., the number of residues that are involved in the β sheet regions. The current model of the parallel D23N fibril structure shows a smaller hydrophobic core, relative to the wild-type sequence, that does not include residues G37–V40 and becomes further reduced in the antiparallel structure for the same mutant (Qiang et al., 2012). On the other hand, shorter segments of wild-type Aβ sequence with a much smaller hydrophobic core, containing either the C- (K16–E22) or N-terminal (A30–V40) amyloidogenic regions, form fibrils with predominantly antiparallel β sheet structures (Balbach et al., 2000; Lansbury et al., 1995). However, the full-length wild-type Aβ sequence forms exclusively parallel, in-register β sheet fibrils with an extensive core region spanning up to the C-terminal residue V40. Taken together, these results suggest that Aβ has a higher propensity to form antiparallel fibrils as a result of sequence mutations that limit the size of the hydrophobic core region. On the other hand, a parallel, in-register β sheet arrangement is strongly favored by the optimization of hydrophobic interactions involving a more extended steric zipper motif.

The availability of multiple Aβ fibril structures now permits a more complete characterization of the end-points of different fibril formation pathways. Comparison of the three structures (wild-type Aβ, parallel, and antiparallel Aβ D23N) suggests a correlation between the D23N mutation, the luminal side-chain orientation of K28, and the absence of C-terminal residues in the hydrophobic core (Figure 6). While a stabilizing D23–K28 salt bridge is observed in the wild-type structure, in the D23N mutant the hydrophobic core can no longer accommodate the charged side chain of K28 that is now a solvent-exposed orientation. Our NMR experiments did not directly verify the formation of a stable K28–V40 salt bridge interaction, suggesting that the charges of K28 and V40 are instead fully solvated. However, our results do not exclude the possibility of a transient electrostatic interaction between the two sites, especially at the early stages of fibril formation. Using saturation-transfer NMR experiments reporting on fibril formation kinetics in solution (Fawzi et al., 2012) and structural characterization of the final fibril structures by solid-state NMR, the role of different familiar AD sequence mutations in stabilizing distinct metastable intermediates along the fibril formation pathway can be achieved.

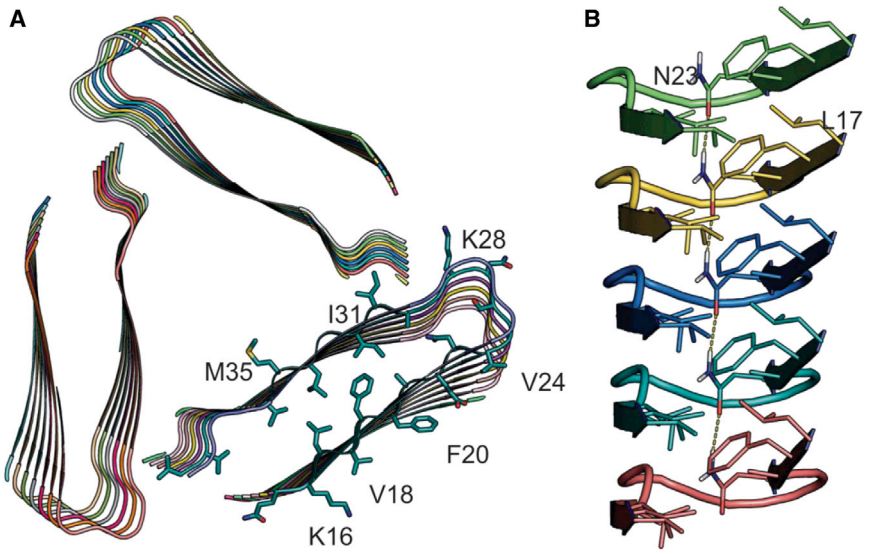

Figure 5. Representative Structural Model of the Parallel, In-Register Fibril of the D23N Iowa Mutant of Aβ

(A) Top view along the fibril and 3-fold symmetry axes. The side chains of a single subunit are shown, highlighting the steric-zipper core formed by residues L17, F19, and A21 from the N-terminal and I32, L34, and V36 from the C-terminal β strands. The loop conformation shows a luminal placement of residues N23 and S26, while N27 and K28 are oriented toward the solvent.

(B) Lateral view of a single cross-β subunit extracted from the 3-fold bundle along the main fibril axis. The staggered arrangement of β strands from individual subunits and hydrogen-bonding network formed by the side chain of N23 are highlighted on the structure.

EXPERIMENTAL PROCEDURES

Preparation of Parallel D23N Fibril Samples

D23N $A\beta_{1-40}$ was synthesized using solid phase peptide synthesis (Applied Biosystems 433A automated peptide synthesizer) with fluorenylmethyloxycarbonyl chloride chemistry and purified by high-performance liquid chromatography equipped with a C3 reverse phase column (Zorbax, Agilent), using a H2O/acetonitrile gradient with 1.0% acetic acid. The mass of peptides was verified by electrospray ionization mass spectrometry (1100 MSD, Hewlett-Packard). The purified product (>95% p.m.) was lyophilized and stored at −20°C to prevent the oxidation and aggregation of monomer before fibrillation.

Toward preparing parallel fibrils, the lyophilized peptide was first dissolved in DMSO to a starting concentration of 5.0 mM, and the DMSO solution was then diluted into phosphate buffer (10 mM, *p*H = 7.4, 0.01% NaN_3) to a final peptide concentration of 100 μM. This peptide solution was incubated at 4°C for 1 week, until the formation of fibrils could be verified using negatively stained TEM. We used a relatively lower temperature of 4°C (comparing with the ambient temperature or 37°C) such that the experimental conditions were consistent with those used previously to prepare antiparallel fibrils (Qiang et al., 2012). After 1 week of incubation, 10% of the fibril solution was sonicated for 2 min on an ice bath to form seeds (i.e., short fibril fragments of ~100 nm in length), and 100 μM fresh D23N $A\beta_{1-40}$ monomer solution was added to the seeds. The mixture was then incubated at 4°C for 4 hr to allow the elongation of seeded fibrils, which was verified by TEM. This sonication-incubation procedure was repeated for eight cycles, and the final product was collected by ultracentrifugation (100,000 round-per-minutes, 432,000 × *g*, Beckmann Coulter). As opposed to the protocol used previously to prepare antiparallel D23N mutant fibrils (Qiang et al., 2012), the current procedure did not involve the filtration step, which separated filaments based on their size. By using a shorter incubation time during the repeated seeding, the current protocol selectively amplifies filaments that elongate more rapidly (Qiang et al., 2011).

TEM

TEM measurements were performed using an FEI Morgagni microscope, operating at 80 kilovolts. To obtain each negatively stained TEM image, a 10 μl drop of 25 μM fibril solution was deposited onto a glow-discharged carbon film, which was supported by lacey carbon on a 300 mesh copper TEM grid. The fibril solution was absorbed for 2 min and then removed by a tissue paper. The grid was then rinsed once with 10 μl of deionized water and then stained with 10 μl of 2% uranyl acid for 30–40 s. The staining solution was then removed, and the grid was dried in air before measurement. All negatively stained TEM images were recorded using 89,000× magnification. For mass-per-length (MPL) measurements (Chen et al., 2009), a 5 μl drop of 10 μM fibril solution was mixed with 5 μl of tobacco mosaic virus (TMV) solution (0.5 mg/mL in *p*H 8.0 Tris buffer). The mixture was deposited on glow-discharged grid and absorbed for 2 min. The solution was removed by tissue paper, and the grid was rinsed once with deionized water and dried in the air before examination. Dark-field images were recorded using 44,000× magnification with a 1.2° tilt of the electron beam. The beam intensity was adjusted so that there was a uniform illumination for each image field. MPL values for individual fibrils were measured by quantification of relative intensities of fibrils and TMV in ~20 image fields. The fibril MPL values were calibrated using the standard MPL value for TMV (131 kilodaltons/nm).

Solid-State NMR

For NMR measurements, D23N $A\beta_{1-40}$ fibrils pellets were collected from the incubation solution using ultracentrifugation at 435,000 × *g* and 4°C for 60 min. The wet pellet was then freeze-dried, packed into magic angle spinning (MAS) rotors with additional Teflon spacers, and rehydrated with 1 μL/mg of deionized water for NMR measurements.

Solid-state NMR measurements were performed at either 9.4 T (100.4 MHz ^{13}C NMR frequency) or 14.1 T (150.6 MHz ^{13}C NMR frequency) with a Varian InfinityPlus spectrometer and a Varian 3.2 mm triple-resonance MAS probe, or with a Bruker Avance III spectrometer and a 2.5 mm TriGamma MAS probe. For all the experiments, the initial ^{13}C signal was generated by a 90° ^{1}H flip pulse followed by a ^{1}H-^{13}C cross polarization (CP) period. The ^{13}C field during CP was centered at ~50 kHz with an adiabatic (on Varian spectrometer) or a linear (on Bruker spectrometer) ramp of ~25 kHz. The ^{1}H field was optimized accordingly for different experiments so that the Hartmann-Hahn condition was always satisfied. For the fpRFDR experiments (Ishii, 2001), the mixing period was set to 2.4 milliseconds (ms) and was composed of a series of rotor-synchronized π pulses with 15.0 μs pulse widths. There was a two-pulse phase-modulation (TPPM) decoupling with 100 kHz ^{1}H radiofrequency (rf) field that was utilized during the t_1 and t_2 periods. For the PITHIRDS-CT experiments that detected the intermolecular ^{13}C-^{13}C dipole-dipole couplings (Tycko, 2007), the MAS frequency was set to 20.0 kHz and the ^{13}C π pulses during the dephasing period were set to 16.7 μs, which was 1/3 of the rotor period. The pulsed spin locking (PSL) approach was used for the acquisition period in order to achieve enhancement in the spectral sensitivity (Petkova and Tycko, 2004). A reduced ^{1}H TPPM decoupling field of ~75 kHz was utilized during the PSL acquisition time. For the proton-assisted spin diffusion (RAD) experiments, which provide long-range side-chain or backbone contacts up to 7 Å (Morcombe et al., 2004), a 500 ms mixing period was applied and the ^{1}H rf field during the mixing period was set to be ~10 kHz, which is close to the MAS frequency. All these 2D experiments were ^{13}C detected. The ^{13}C chemical shifts were referenced relative to tetramethylsilane, using the carbonyl signal of L-alanine powder at 177.95 parts per million (ppm) as an external reference.

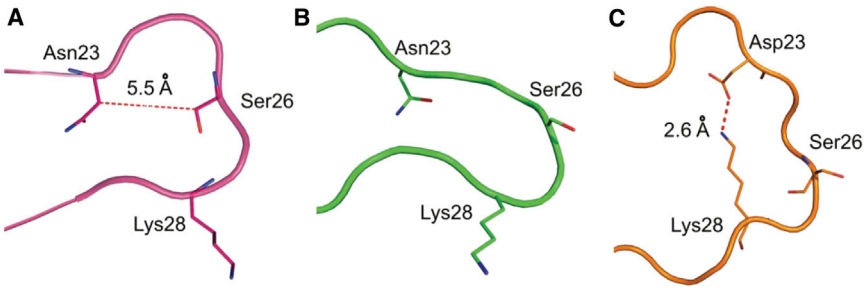

Figure 6. Side-Chain Orientations of the Loop Region Residues
The residues Asn23/Asp23, Ser26, and Lys28 were shown in (A) D23N parallel (PDB ID 2MPZ), (B) D23N antiparallel (PDB ID 2LNQ), and (C) wild-type parallel Aβ fibrils (PDB ID 2M4J). Solid-state NMR experimental distance restraints were obtained between specific nuclei within residue pairs Asn23/Ser26 in model (A) and Asp23/Lys28 in model (C).

Structure Calculations Using Rosetta

We used the Rosetta symmetric modeling framework (DiMaio et al., 2011), customized for optimal sampling of parallel fibril arrangements (see Supplemental Experimental Procedures for a complete description of symmetry parameters and command lines). In general, the use of an explicitly symmetric representation of the system has two main advantages over conventional approaches relying on noncrystallographic symmetry restraints to enforce symmetry during a calculation: (1) the rigid-body parameters of the system can be manipulated individually, allowing for optimal sampling of conformations consistent with a specified symmetry type; and (2) only a minimum subset of the full system needs to be considered for energy and derivative evaluation. Conformational changes are then automatically propagated among symmetry-related subunits at no additional overhead.

The Rosetta structure calculations were done for the Aβ segments 16–40, as these residues are located in the fibril core based on previous studies (Paravastu et al., 2008; Petkova et al., 2006). Briefly, the solid-state chemical shifts were used to select 3- and 9-residue fragments from a database of high-resolution X-ray structures that was further annotated by predicted chemical shift values for backbone atoms using the program SPARTA+ (see Supplemental Experimental Procedures step, fragment selection) (Shen and Bax, 2010; Vernon et al., 2013). Starting from an array of extended polypeptide chains arranged around a 3-fold axis of symmetry axis that is parallel to the main axis of the fibril, we performed symmetric fold-and-dock calculations using the chemical shift-derived fragments and solid-state NMR restraints as described previously (Loquet et al., 2012). The fold-and-dock protocol consists of two main steps. In the first step ("*Abinitio*"), performed using a coarse-grain representation of the system, fragment insertion and rigid-body Monte Carlo trials are propagated among symmetry-related subunits and scored using a knowledge-based centroid energy function that favors collapsed conformations with protein-like features. The second step ("*Relax*") gradually transforms the previously sampled coarse-grain models into realistic, all-atom fibril assemblies in a series of iterations, involving symmetric side-chain repacking and quasi-*Newton* minimization of the total energy of the system, by optimizing all side-chain, backbone, and rigid-body degrees of freedom. At this final step, we are using a physically realistic, all-atom energy function (talaris2013). The talaris2013 score function combines several recent improvements, including the 2010 Dunbrack Rotamer Library, the sp^2 hydrogen bond potential, an explicit electrostatics term with a distance dependent dielectric, the use of bicubic-spline interpolation of all knowledge-based potentials, an improved disulfide potential, and an analytic evaluation of Lennard-Jones and EEF1 potentials. The detailed functional form of the energy function is outlined in detail in previous work (Leaver-Fay et al., 2013; Song et al., 2011).

We modeled a total of nine trimeric units, helically arranged to yield a 27-subunit fibril. In all calculations, the 3-fold and overall fibril symmetry parameters (degree rotation and axial displacements per unit layer, plus radii of the 2- and 3-fold symmetry axes) were sampled according to the experimental restraints and Rosetta energy function. We computed a total of 10,000 models with an approximate central processing unit time of 3 min/model.

The following types of experimental distance restraints from solid-state NMR measurements were used (cf. Table S1): (1) intramolecular backbone and side-chain contacts from the assigned crosspeaks in 2D ^{13}C-^{13}C spin diffusion spectra; (2) intermolecular contacts within the trimeric Aβ unit located in the same layer; and (3) quantitative ^{13}C-PITHIRDs-CT distances reporting on contacts between adjacent Aβ monomers along the fibril axis. All restraints were implemented using a flat-bottom potential as a parametric function of the distance x (in Å) between two interacting atoms:

$$E(x) = \begin{cases} 0, & x \geq ll \cap x \leq ul \\ 2^{(x-ul)/0.3}, & x > ul \\ 2^{(ll-x)/0.3}, & x < ll \end{cases},$$

with a lower limit (ll) of 1.5 Å and an upper limit (ul) proportional to

$$\left(Ix/I_0\right)^{-1/6},$$

where Ix is the cross peak height and I_0 the height of the diagonal peak (Manolikas et al., 2008). Judged from the spectral noise in the 2D spin diffusion experiments, which had roughly 10:1 signal-to-noise ratio for the strongest long-range crosspeak between the C^{ζ} of F19 and C^{γ} of L34, our upper-limit distance estimation gave ~0.1 Å uncertainty for the strongest interresidue crosspeak with

$$\left(Ix/I_0\right) \approx 0.3$$

and ~0.6 Å uncertainty for the weakest interresidue crosspeak with

$$\left(Ix/I_0\right) \approx 0.1.$$

The F19/L34 crosspeak was used as an internal calibration point assuming a 6.5 Å distance, as observed in preliminary calculations where all restraints were assigned a "generous" 10 Å upper limit. The average value of sampled distances for the strongest contact (between the C^{ζ} of F19 and C^{γ} of L34) was then used as an estimate to calibrate the remaining restraints in the final calculations. This approach prevents over-restraining the calculations to the NMR data. Given that the majority (>80%) of the final score is determined by the Rosetta energy terms, the exact upper value did not have a significant effect on the sampled models. With the exception of a single outlier (V24C'/G29Cα, cf. Figure S1), the distances obtained in the final models are within the estimated upper limits. The violation for V24C'/G29Cα is due to severe signal overlap in the diagonal region for the carbonyl of V24, which prevents the precise estimation of the upper limit.

ACCESSION NUMBERS

The PDB accession number for the parallel-in-register Iowa mutant fibril structure reported in this paper is 2MPZ.

SUPPLEMENTAL INFORMATION

Supplemental Information includes seven figures and two tables and can be found with this article online at http://dx.doi.org/10.1016/j.str.2014.10.022.

ACKNOWLEDGMENTS

This work is supported by the National Institute of Diabetes, Digestive, and Kidney Disease and the National Institute of Allergy and Infectious Diseases Intramural Research Programs; the Intramural AIDS-Targeted Antiviral

Program of the Office of the Director; the NIH; and the Research Foundation at the State University of New York. Part of the solid-state NMR measurements was supported by the National Science Foundation Major Instrumentation Program (NSF 0922815). We greatly appreciate the support from Dr. Robert Tycko and Dr. David Baker on materials, instrumentation and computation time, and helpful discussion. We thank Dr. Frank DiMaio for useful discussions.

Received: July 11, 2014
Revised: October 7, 2014
Accepted: October 31, 2014
Published: December 24, 2014

REFERENCES

Ahmed, M., Davis, J., Aucoin, D., Sato, T., Ahuja, S., Aimoto, S., Elliott, J.I., Van Nostrand, W.E., and Smith, S.O. (2010). Structural conversion of neurotoxic amyloid-beta(1-42) oligomers to fibrils. Nat. Struct. Mol. Biol. *17*, 561–567.

Antzutkin, O.N., Balbach, J.J., Leapman, R.D., Rizzo, N.W., Reed, J., and Tycko, R. (2000). Multiple quantum solid-state NMR indicates a parallel, not antiparallel, organization of beta-sheets in Alzheimer's beta-amyloid fibrils. Proc. Natl. Acad. Sci. USA *97*, 13045–13050.

Antzutkin, O.N., Leapman, R.D., Balbach, J.J., and Tycko, R. (2002). Supramolecular structural constraints on Alzheimer's beta-amyloid fibrils from electron microscopy and solid-state nuclear magnetic resonance. Biochemistry *41*, 15436–15450.

Balbach, J.J., Ishii, Y., Antzutkin, O.N., Leapman, R.D., Rizzo, N.W., Dyda, F., Reed, J., and Tycko, R. (2000). Amyloid fibril formation by A beta(16-22), a seven-residue fragment of the Alzheimer's beta-amyloid peptide, and structural characterization by solid state NMR. Biochemistry *39*, 13748–13759.

Barrett, P.J., Song, Y.L., Van Horn, W.D., Hustedt, E.J., Schafer, J.M., Hadziselimovic, A., Beel, A.J., and Sanders, C.R. (2012). The amyloid precursor protein has a flexible transmembrane domain and binds cholesterol. Science *336*, 1168–1171.

Benzinger, T.L.S., Gregory, D.M., Buekoth, T.S., Miller-Auer, H., Lynn, D.G., Botto, R.E., and Meredith, S.C. (1998). Propagating structure of Alzheimer's beta-amyloid (10-35) is parallel beta-sheet with residues in exact register. Proc. Natl. Acad. Sci. USA *95*, 13407–13412.

Bertini, I., Grnnelli, L., Luchinat, C., Mao, J.F., and Nesi, A. (2011). A new structural model for A beta(40) fibrils. J. Am. Chem. Soc. *133*, 16013–16022.

Chen, B., Thurber, K.R., Shewmaker, F., Wickner, R.B., and Tycko, R. (2009). Measurement of amyloid fibril mass-per-length by tilted-beam transmission electron microscopy. Proc. Natl. Acad. Sci. USA *106*, 14339–14344.

Chiti, F., and Dobson, C.M. (2006). Protein misfolding, functional amyloid, and human disease. Annu. Rev. Biochem. *75*, 333–366.

Colletier, J.P., Laganowsky, A., Landau, M., Zhao, M.L., Soriaga, A.B., Goldschmidt, L., Flot, D., Cascio, D., Sawaya, M.R., and Eisenberg, D. (2011). Molecular basis for amyloid-beta polymorphism. Proc. Natl. Acad. Sci. USA *108*, 16938–16943.

Cornell, W.D., Cieplak, P., Bayly, C.I., Gould, I.R., Merz, K.M., Ferguson, D.M., Spellmeyer, D.C., Fox, T., Caldwell, J.W., and Kollman, P.A. (1995). A second generation force field for the simulation of proteins, nucleic acids, and organic molecules. J. Am. Chem. Soc. *117*, 5179–5197.

Das, R., Andre, I., Shen, Y., Wu, Y.B., Lemak, A., Bansal, S., Arrowsmith, C.H., Szyperski, T., and Baker, D. (2009). Simultaneous prediction of protein folding and docking at high resolution. Proc. Natl. Acad. Sci. USA *106*, 18978–18983.

DiMaio, F., Leaver-Fay, A., Bradley, P., Baker, D., and Andre, I. (2011). Modeling symmetric mocaromolecular structures in Rosetta3. PLoS ONE *6*, e20450.

Fawzi, N.L., Ying, J., Torchia, D.A., and Clore, G.M. (2012). Procing exchange kinetics and atomic resolution dynamics in high-molecular-weight complexes using dark-state exhange saturation transfer NMR spectroscopy. Nat. Protoc. *7*, 1523–1533.

Guntert, P. (2004). Automatic NMR protein structure calculation with CYANA. Methods Mol. Biol. *278*, 353–378.

Ishii, Y. (2001). 13C-13C dipolar recoupling under very fast magic angle spinning in solid-state nuclear magnetic resonance: Application to distance measurements, spectral assignments, and high-throughput secondary-structure determination. J. Chem. Phys. *114*, 8473–8483.

Karran, E., Mercken, M., and De Strooper, B. (2011). The amyloid cascade hypothesis for Alzheimer's disease: an appraisal for the development of therapeutics. Natl. Rev. *10*, 698–712.

Kayed, R., Head, E., Thompson, J.L., McIntire, T.M., Milton, S.C., Cotman, C.W., and Glabe, C.G. (2003). Common structure of soluble amyloid oligomers implies common mechanism of pathogenesis. Science *300*, 486–489.

Ladiwala, A.R.A., Bhattacharya, M., Perchiacca, J.M., Cao, P., Raleigh, D.P., Abedini, A., Schmidt, A.M., Varkey, J., Langen, R., and Tessier, P.M. (2012). Rational design of potent domain antibody inhibitors of amyloid fibril assembly. Proc. Natl. Acad. Sci. USA *109*, 19965–19970.

Lansbury, P.T., Costa, P.R., Griffiths, J.M., Simon, E.J., Auger, M., Halverson, K.J., Kocisko, D.A., Hendsch, Z.S., Ashburn, T.T., Spencer, R.G.S., et al. (1995). Structural model for the beta-amyloid fibril based on interstrand alignment of an antiparallel-sheet comprising a C-terminal peptide. Nat. Struct. Biol. *2*, 990–998.

Leaver-Fay, A., Tyka, M., Lewis, S.M., Lange, O.F., Thompson, J., Jacak, R., Kaufman, K., Renfrew, P.D., Smith, C.A., Sheffler, W., et al. (2011). ROSETTA3: an object-oriented software suite for the simulation and design of macromolecules. Methods Enzymol. *487*, 545–574.

Leaver-Fay, A., O'Meara, M.J., Tyka, M., Jacak, R., Song, Y., Kellogg, E.H., Thomson, J., Davis, I.W., Pache, R.A., Lyskov, S., et al. (2013). Scientific benchmarks for guiding macromolecular energy function improvement. Methods Enzymol. *523*, 109–143.

Loquet, A., Sgourakis, N.G., Gupta, R., Giller, K., Riedel, D., Goosmann, C., Griesinger, C., Kolbe, M., Baker, D., Becker, S., and Lange, A. (2012). Atomic model of the type III secretion system needle. Nature *486*, 276–279.

Lu, J.X., Qiang, W., Yau, W.M., Schwieters, C.D., Meredith, S.C., and Tycko, R. (2013). Molecular structure of beta-amyloid fibrils in Alzheimer's disease brain tissue. Cell *154*, 1257–1268.

Luhrs, T., Ritter, C., Adrian, M., Riek-Loher, D., Bohrmann, B., Dobeli, H., Schibert, D., and Riek, R. (2005). 3D structure of Alzheimer's amyloid-b(1-42) fibrils. Proc. Natl. Acad. Sci. USA *102*, 17342–17347.

Manolikas, T., Herrmann, T., and Meier, B.H. (2008). Protein structure determination from 13C spin-diffusion solid-state NMR spectrosocpy. J. Am. Chem. Soc. *130*, 3959–3966.

Mason, R.P., Estermyer, J.D., Kelly, J.F., and Mason, P.E. (1996). Alzheimer's disease amyloid beta peptide 25-35 is localized in the membrane hydrophobic core: X-ray diffraction analysis. Biochem. Biophys. Res. Commun. *222*, 78–82.

Mason, R.P., Jacob, R.F., Walter, M.F., Mason, P.E., Avdulov, N.A., Chochina, S.V., Igbavboa, U., and Wood, W.G. (1999). Distribution and fluidizing action of soluble and aggregated amyloid beta-peptide in rat synaptic plasma membranes. J. Biol. Chem. *275*, 18801–18807.

Morcombe, C.R., Gaponenko, V., Byrd, R.A., and Zilm, K.W. (2004). Diluting abundant spins by isotope edited radio frequency fild assisted diffusion. J. Am. Chem. Soc. *126*, 7196–7197.

O'Brien, R.J., and Wong, P.C. (2011). Amyloid precursor protein processing and Alzheimer's disease. Annu. Rev. Neurosci. *34*, 185–204.

Paravastu, A.K., Leapman, R.D., Yau, W.M., and Tycko, R. (2008). Molecular structural basis for polymorphism in Alzheimer's beta-amyloid fibrils. Proc. Natl. Acad. Sci. USA *105*, 18349–18354.

Peters, I., Igbaaboa, U., Schuett, T., Haidari, S., Hartig, U., Rosello, X., Boettner, S., Copanaki, E., Deller, T., Koegel, D., et al. (2009). The interaction of beta-amyloid peotein with cellular membrane stimulates its own production. Biochim. Biophys. Acta. Biomembr. *1788*, 964–972.

Petkova, A.T., and Tycko, R. (2004). Sensitivity enhancement in structural measurements by solid state NMR through pulsed spin locking. J. Magn. Reson. *155*, 293–299.

Petkova, A.T., Ishii, Y., Balbach, J.J., Antzutkin, O.N., Leapman, R.D., Delaglio, F., and Tycko, R. (2002). A structural model for Alzheimer's beta-amyloid fibrils

based on experimental constraints from solid state NMR. Proc. Natl. Acad. Sci. USA *99*, 16742–16747.

Petkova, A.T., Leapman, R.D., Guo, Z.H., Yau, W.M., Mattson, M.P., and Tycko, R. (2005). Self-propagating, molecular-level polymorphism in Alzheimer's beta-amyloid fibrils. Science *307*, 262–265.

Petkova, A.T., Yau, W.M., and Tycko, R. (2006). Experimental constraints on quaternary structure in Alzheimer's beta-amyloid fibrils. Biochemistry *45*, 498–512.

Petrassi, H.M., Klabunde, T., Sacchettini, J., and Kelly, J.W. (2000). Structure-based design of N-phenoxazine transthyretin amyloid fibril inhibitors. J. Am. Chem. Soc. *122*, 2178–2192.

Qiang, W., Yau, W.M., and Tycko, R. (2011). Structural evolution of Iowa mutant b-amyloid fibrils from polymorphic to homogeneous states under repeated seeded growth. J. Am. Chem. Soc. *133*, 4018–4029.

Qiang, W., Yau, W.M., Luo, Y.Q., Mattson, M.P., and Tycko, R. (2012). Antiparallel beta-sheet architecture in Iowa-mutant beta-amyloid fibrils. Proc. Natl. Acad. Sci. USA *109*, 4443–4448.

Reddy, G., Straub, J.E., and Thirumalai, D. (2009). Influence of preformed Asp23-Lys28 salt bridge on the conformational fluctuations of monomers and dimers of Abeta peptides with implications for rates of fibril formation. J. Phys. Chem. B *113*, 1162–1172.

Sawaya, M.R., Sambashivan, S., Nelson, R., Ivanova, M.I., Sievers, S.A., Apostol, M.I., Thompson, M.J., Balbirnie, M., Wiltzius, J.J., McFarlane, H.T., et al. (2007). Atomic structure of amyloid cross-beta spines reveal varied steric zipper. Nature *447*, 453–457.

Schwieters, C.D., Kuszewski, J.J., Tjandra, N., and Clore, G.M. (2003). The Xplor-NIH NMR molecular structure deermination package. J. Magn. Reson. *160*, 65–73.

Selkoe, D.J. (1991). The molecular pathology of Alzheimer's disease. Neuron *6*, 487–498.

Shen, Y., and Bax, A. (2010). SPARTA+: a modest improvement in emprical NMR chemical shift prediction by means of an artificial neural network. J. Biomol. NMR *48*, 13–22.

Shen, Y., Delaglio, F., Cornilescu, G., and Bax, A. (2009). TALOS+: A hybrid method for predicting protein backbone torsion angles from NMR chemical shifts. J. Biomol. NMR *44*, 213–223.

Siepe, J.D., Benson, M.D., Buxbaum, J.N., Ikeda, S., Merlini, G., Saraiva, M.J., and Westermark, P. (2012). AMyloid fibril protein namenclature: 2012 recommendations of the nomenclature committee of the intl Soc Amyloidosis. Amyloid *19*, 167–170.

Sievers, S.A., Karanicolas, J., Chang, H.W., Zhao, A., Jiang, L., Zirafi, O., Stevens, J.T., Munch, J., Baker, D., and Eisenberg, D. (2011). Structure-based design of non-natural amino-acid inhibitors of amyloid fibril formation. Nature *475*, 96–117.

Skora, L., and Zweckstetter, M. (2012). Determination of amyloid core structure using chemical shifts. Protein Sci. *21*, 1948–1953.

Song, Y., Tyka, M., Leaver-Fay, A., Thompson, J., and Baker, D. (2011). Structure-guide forcefield optimization. Proteins *79*, 1898–1909.

Sunde, M., Serpell, L.C., Bartlam, M., Fraser, P.E., Pepys, M.B., and Blake, C.C. (1997). Common core structure of amyloid fibrils by synchrotron X-ray diffraction. J. Mol. Biol. *273*, 729–739.

Tarus, B., Straub, J.E., and Thirumalai, D. (2006). Dynamics of Asp23-Lys28 salt bridge formation in Abeta10-35 monomers. J. Am. Chem. Soc. *128*, 16159–16168.

Tycko, R. (2007). Symmetry-based constant-tiome homonuclear dipolar recoupling in solid state NMR. J. Chem. Phys. *126*, 064506.

Tycko, R. (2011). Solid-state NMR studies of amyloid fibril structure. Annu. Rev. Phys. Chem. *62*, 279–299.

Tycko, R., Sciarretta, K.L., Orgel, J.P.R.O., and Meredith, S.C. (2009). Evidence for novel beta-sheet structures in Iowa mutant beta-amyloid fibrils. Biochemistry *48*, 6072–6084.

Vernon, R., Shen, Y., Baker, D., and Lange, O.F. (2013). Improved chemical shift based fragment selection for CS-Rosetta using Rosetta3 fragment picker. J. Biomol. NMR *57*, 117–127.

Widenbrant, M.J.O., Rajadas, J., Sutardja, C., and Fuller, G.G. (2006). Lipid-induced beta-amyloid peptide assemblage fragmentation. Biophys. J. *91*, 4071–4081.

Wishart, D.S., Bigam, C.G., Yao, J., Abildgaard, F., Dyson, J., Oldfield, E., Markley, J.L., and Sykes, B.D. (1995). 1H, 13C and 15N chemical shift referencing in biomolecular NMR. J. Biomol. NMR *6*, 135–140.